AIAA SciTech Forum
6-10 January 2025, Orlando, FL
AIAA SCITECH 2025 Forum

10.2514/6.2025-1746

Design of Functionally Graded Inconel 718 Alloy Structures by Developing Material Property Closures

Md Maruf Billah* and Pınar Acar†
Virginia Tech, Blacksburg, 24061, VA, USA

Inconel 718 stands out as a prominent member of the nickel-based superalloys within the Inconel family. This study focuses on determining the property closures of stiffness parameters of polycrystalline Inconel 718 alloy under variations in its microstructural texture. The orientation distribution function, as a one-point probability descriptor, is used to delineate the microstructural texture. Concurrently, the effects of the uncertainty of single-crystal properties and microstructural texture on the property closures are analyzed. A few examples of functionally graded structures are proposed using the material property closures obtained for the Inconel 718 alloy by setting the primary objective to increase dimensional stability under specific loading conditions. In particular, two design cases are explored: single-variable instances such as the design of axially graded beams and columns, and the dual-variable scenarios of designing radially graded pressurized cylinders. For single-variable cases, the Rayleigh-Ritz methodology is employed to derive property functions, while for dual-variable cases, linear trade-off functions are meticulously proposed based on stress distributions.

Nomenclature

χ	Single-crystal property
ϵ	Components of strain tensor
ω	Integration weight
σ	Components of stress tensor
$\mathbf{A}$	Orientation distribution function
$\mathbf{r}$	Rodrigues orientation vector
C	Parameters of stiffness tensor
E	Modulus of elasticity
F	Applied force
I	Moment of inertia
J	Jacobian
p	Applied pressure
U	Rayleigh-Ritz potential
u	Deflection

---

*Graduate Teaching Assistant, Ph.D. Student, Department of Mechanical Engineering, AIAA Student Member

†Associate Professor, Department of Mechanical Engineering, AIAA Member

I. Introduction

Functionally graded materials (FGMs) can be classified as materials with properties varying along one or more directions to enhance the target performance of structures. Recently, there has been a growing interest in FGMs within the field of additive manufacturing, where properties can be manipulated by adjusting microstructural texture, constituents, or compositions [1, 2]. This capability opens the door to fabricating intricate FGMs characterized by multidimensional and directional gradient architectures, all achievable through tailored process conditions. Inconel 718 (IN-718) is a nickel-based superalloy mainly composed of chromium, nickel, and iron, with adjusted amounts of aluminum, molybdenum, and titanium which provides corrosion-resistance and high-strength [3]. It has several important applications in various industries particularly in aerospace, oil and gas, and chemical processing owing to its exceptional properties [4, 5]. IN-718 exhibits flexibility in FGM production through the variations in microstructural grain orientations. In this work, the material property closures of IN-718 for stiffness parameters have been developed by a finite element discretization method, where the orientation distribution functions (ODFs) quantifying the microstructural texture are varied within the constraints. The ODF is a probabilistic approach for modeling microstructural texture and compute texture-dependent properties [6].

The previous work [7, 8] utilized linear programming and machine learning algorithms to determine the property closures of face-centered cubic (FCC)-Aluminum and hexagonal close-packed (HCP)-Titanium microstructures by utilizing the ODF approach. Furthermore, Acar [9] developed another analytical approach to quantify the randomness in microstructures and its impact on material properties. By integrating an analytical uncertainty quantification algorithm with linear programming, the full spectrum of possible material properties under uncertainty was determined. This methodology was applied to predict stiffness parameters for α-Titanium and a range of multiphysics parameters, including stiffness, yield strength, and magnetostrictive strain, for Galfenol. Researchers have made strides in extending the first-order theory of microstructure design to incorporate morphological texture, paving the way for the development of combined property closures and second-order microstructure design [10]. A subsequent study [11] enhanced the microstructure-sensitive design framework by integrating second-order homogenization theories, which utilize two-point spatial correlations to predict effective properties within the microstructure. Proust and Kalidindi [12] provided a comprehensive guide for researchers and designers to illustrate first-order elasto-plastic property closures, highlighting the critical role of crystallographic texture in influencing the yield and elastic properties of cubic polycrystalline metals. In a similar vein, Landry and Knezevic [13] introduced a computational approach leveraging fast Fourier transforms (FFTs) to establish elastic property closures for HCP metals. Their methodology involved creating a directory of non-zero Fourier transforms for each elastic stiffness tensor component, calculating Fourier transforms of ODFs, and determining ODF-to-elastic property bounds in Fourier space. Recent research has also explored the application of convolutional neural networks (CNNs) to predict effective properties and generate property closures. By harnessing two-point spatial correlations of voxelated eigen-microstructures, this CNN architecture offers a promising avenue for advancing microstructure design and property prediction [14].

Also, several recent experimental studies have explored the production of single-component Ni-based superalloy parts using additive manufacturing techniques [15–18]. Despite these advancements, the investigation of functional grading within such components remains relatively underexplored. Notably, selective laser melting produced parts exhibit promising mechanical properties [19, 20], yet they are also characterized by significant anisotropy due to the directional columnar grain growth inherent in this process [21, 22]. The texture of these materials plays a crucial role in their mechanical performance, as evidenced by research on Ni-based single-crystal superalloys [23, 24]. These studies highlight that mechanical properties, including fatigue life and creep resistance, vary significantly with crystallographic orientation [24]. In particular, orientations with lower stiffness tend to demonstrate longer fatigue life and improved creep strength under tensile loading [24]. As a result, the (001) crystallographic direction, known for its low stiffness, is favored in gas turbine blade applications. Furthermore, Popovich et al. [16] have demonstrated that IN-718 functionally graded components can exhibit controlled transitions in microstructure, texture, and properties across various length scales. By tailoring the fabrication process, it is possible to achieve specific functional gradients that cater to the requirements of different applications.

A significant amount of research was performed to prove that the functionally graded materials can improve the structural performance [25–27]. Closed-form solutions for the stress and displacement distributions within functionally graded spherical vessels and hollow cylinders were derived by Tutuncu and Ozturk [28] under solely internal uniform pressure by utilizing the infinitesimal theory of elasticity. The material stiffness gradient following straightforward power law toward the radial direction of the vessel wall was assumed by keeping a constant Poisson's ratio. Later, Woldemichael and Bezzie [29] unveiled the impact of both graded-index and Poisson's ratio on the numerical elastic outcomes of an FGM composed of a thick-walled cylinder subjected to internal pressure within an in-plane strain setting.

Another study conducted by Sburlati [30] for thick-walled internally and externally pressurized cylinders applied an analytical solution. It aimed to compare the outcomes of two scenarios: one involving a fully graded cylinder and the other with partial grading in the internal coating thickness of the cylinder. On the other hand, Ranganathan et al. [31] observed the structural performance of a functionally graded column, where they compared the buckling load for various functions of the modulus of elasticity. The only applied constraint was that the average modulus of elasticity for each case remained equal. They used two methods: the Rayleigh-Ritz method and the linear perturbation method to solve the eigenvalue problem. Some other studies [32–35] explored the effectiveness of functionally graded beam performance at static and dynamic loading conditions where the desired properties of the materials were varied by changing the proportion of fiber/matrix of composites. After this observation, it can be concluded that the functionally graded structures have adequate advantages over the conventional homogeneous structures. However, to the best of the authors' knowledge, there has been a notable lack of comprehensive studies that incorporate the effects of variations in the microstructural texture when designing FGMs.

This study aims to identify the property closures for stiffness parameters of polycrystalline IN-718 by examining variations in microstructural texture. In parallel, it investigates how uncertainties in single-crystal properties and microstructural texture affect these property closures. Finally, several examples of functionally graded structures are proposed by utilizing the property closures computed for IN-718, with the primary objective of enhancing dimensional stability under specific loading conditions. The complete summary of the present study is illustrated in Fig. 1. The left side of the diagram represents the study's workflow, outlining the inputs, outputs, and methodologies involved, while the right side provides a visual representation of the study's key elements.

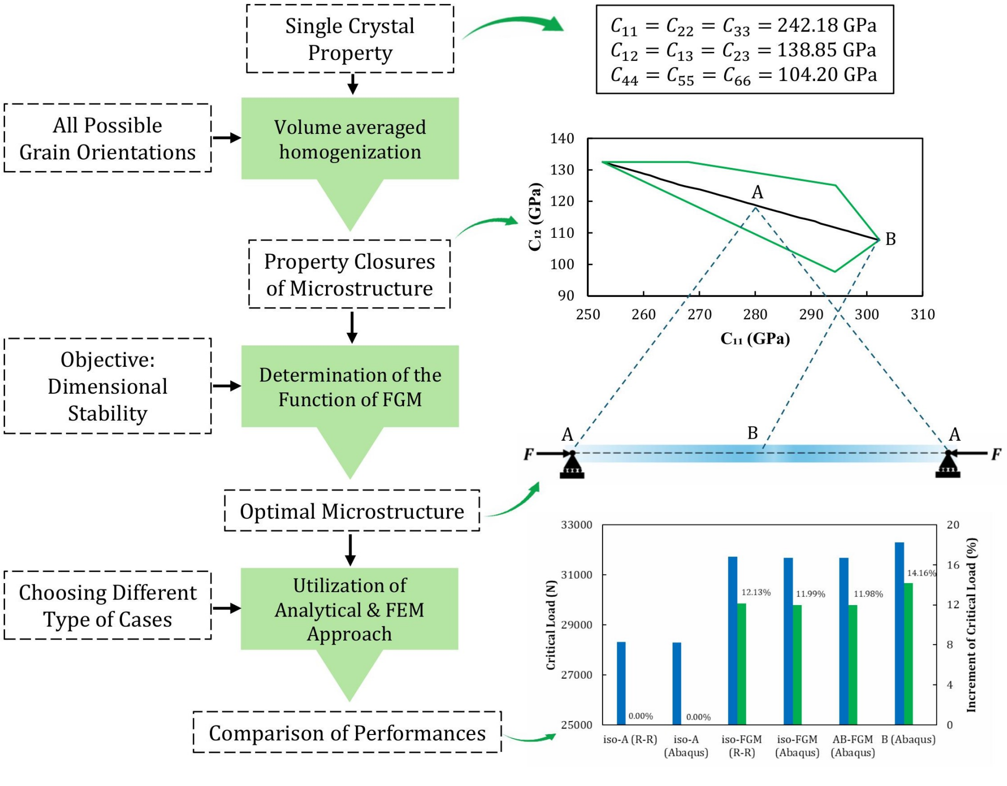

Fig. 1 Comprehensive illustration of study workflow: Input-output framework and methodological overview.

II. Methodology

A. Computation of stiffness properties

In this study, the crystallographic texture of the IN-718 microstructure is represented through the utilization of ODFs. These functions measure the volume densities of various crystallographic orientations in a polycrystalline material and are used to derive homogenized properties. Eventually, the ODFs are defined by several techniques such as Rodrigues parameters [36–38] and Euler angles [39–41]. More precisely, a local finite element discretization method has been employed within the Rodrigues orientation space framework to calculate the homogenized properties in this research. Equation (1) shows the definition of the ODFs ($\mathbf{A}$), focusing on the requirement for crystal volume densities to adhere to a constraint ensuring volume normalization [42]. This approach contains N distinct nodes and N_{elm} finite elements, with each element containing N_{int} integration points. The specific ODF value assigned to each node within the mesh is associated with the volume density of the corresponding crystallographic orientation. The calculation of the orientation-dependent homogenized material property, represented by $< \chi >$, involves utilizing single-crystal property values (χ) together with the nodal point ODFs, as demonstrated in Equation (2). This current study utilizes the isotropic single-crystal stiffness matrix from this referred article [43] where C_{11} = 242.18 GPa, C_{12} = 138.85 GPa, and C_{66} = 104.20 GPa.

$$\int_{\Omega} A(\mathbf{r})dv = \sum_{n=1}^{N_{elm}} \sum_{m=1}^{N_{int}} A(\mathbf{r_m}) w_m |J_n| \frac{1}{(1+\mathbf{r_m}.\mathbf{r_m})^2} = 1 \tag{1}$$

$$\langle \chi \rangle = \int_{\Omega} \chi(\mathbf{r}) A(\mathbf{r}) dv = \sum_{n=1}^{N_{elm}} \sum_{m=1}^{N_{int}} \chi(\mathbf{r_m}) A(\mathbf{r_m})\ w_m |J_n| \frac{1}{(1+\mathbf{r_m}.\mathbf{r_m})^2} \tag{2}$$

B. Property closure formulation

The property closure is a convex space demonstrating all possible values of the selected properties (closure variables) obtainable by feasible microstructure designs. In this study, the property closures for stiffness parameters of IN-718 microstructures are determined using gradient-based optimization. The objective function for a specific property closure of C_{ij} versus C_{kl} is defined as a minimization problem exhibited by Equation (3), where the desired function $f(\mathbf{A})$ has been set as $|C_{ij} - C_{kl}|$ by considering the volume normalization constraint for the ODFs given in Equation (1) and the fundamental non-negativity constraints on ODFs. Later, by increasing and decreasing the magnitude of C_{ij} and C_{kl}, the boundary points of the property closures can be obtained. At this time, the lower bounds ($\mathbf{A}_{lb}$) are null matrix and upper bounds ($\mathbf{A}_{ub}$) are set to the maximum optimal number that reduces the run time. Furthermore, the local maximum and minimum values of the desired stiffness matrix components are determined by adjusting the lower bound ($\mathbf{A}_{lb}$) and upper bound ($\mathbf{A}_{ub}$) values. When the function $f(\mathbf{A})$ has been set as C_{ij} or C_{kl}, the objective function can address both maximization and minimization while the constraints remain unchanged. All ODFs must satisfy the condition of volume normalization within the fundamental region, thus the volume fraction is equal to unity as shown in Equation (1). This constraint can be expressed as a linear equation, $\mathbf{q}^T\mathbf{A}$=1, in terms of the ODF values at nodal points. Using a similar approach, the homogenized material property, which is dependent on orientation and denoted as $< \chi >$, can be calculated using single-crystal property values (χ) and the ODFs at nodal points, as shown in Equation (2). This can also be represented as a linear equation, $< \chi >= \mathbf{p}^T\mathbf{A}$, where $\mathbf{p}$ is the property matrix found using Equation (2).

$$\min_{A} f(\mathbf{A}) = \min \mathbf{p}^T\mathbf{A} \text{ such that} \begin{cases} A \geq 0 \\ \mathbf{q}^T\mathbf{A} = 1 \\ \mathbf{A}_{lb} \leq \mathbf{A} \leq \mathbf{A}_{ub} \end{cases} \tag{3}$$

C. Uncertainty quantification for the property closures

In this study, two sources of microstructural uncertainty are considered: variations in crystallographic texture and single-crystal properties. The texture is characterized by the ODFs ($\mathbf{A}$), which quantifies the volume fraction of crystals in a polycrystalline material oriented in specific directions. The ODF provides a probabilistic framework for representing and adjusting the orientation of grains, where a slight modification in the probability of one orientation influences others. Furthermore, property closures are constructed based on the entire set of possible ODFs. As such, introducing uncertainty in the ODFs or textures is inherently constrained within the bounds of the established property closure. This ensures that any variation in texture remains within the feasible material behavior space defined by the closure. In contrast, uncertainty in single-crystal properties can directly influence the microstructural property closures. A small variation in the property matrix ($\mathbf{p}$) can alter the size and shape of these closures. To simplify this complexity, the variations of the property closures can first be investigated at the corner points. In a two-dimensional space, this approach yields a maximum of four uncertain points, each corresponding to a corner point. These points help define the new closure, accounting for a specific level of uncertainty. Consequently, variations in the property matrix result in two extreme matrices, which manifest as four distinct points for two key stiffness components in the two-dimensional space. This process allows to construct a revised closure that reflects the impact of uncertainty on stiffness parameters.

D. Design of FGM structures

1. FGM design: single-variable case

The single-variable instance includes the axially graded beam and column cases, where the Rayleigh-Ritz method is employed to construct the function of the modulus of elasticity to achieve a specific objective. The Rayleigh-Ritz method is an analytical approach used in structural engineering to approximate the behavior of columns and beams. It involves expressing the energy storage, energy decapitation, and work done; then minimizing the potential energy functional [44]. This method allows efficient approximation of the deflections and stresses in columns and beams under various loading conditions, aiding in the design and analysis of structures as illustrated in Fig. 2. In this current work, pinned-pinned supported column and simply supported beam are analyzed and their corresponding Rayleigh-Ritz potential is expressed in Equations (4) and (6).

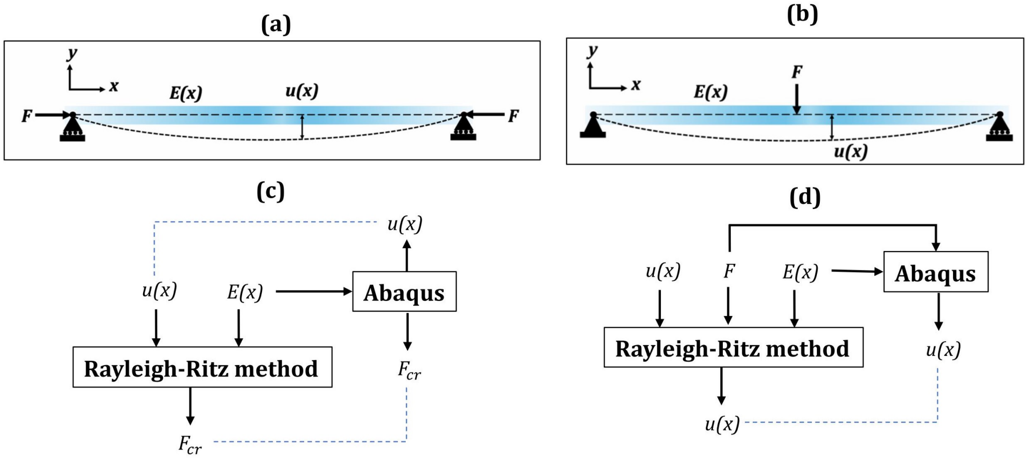

Fig. 2 (a)-(b) Schematic diagram of the pinned-pinned column and simply supported beam; (c)-(d) Brief outline of analytical method and finite element analysis (FEA). The function of displacement and elastic moduli are expressed by $u(x)$ and $E(x)$, whereas F_{cr} and F represent the column critical load of buckling and beam load, respectively.

$$U = \frac{1}{2}\int_0^L E(x)\, I \left(\frac{\partial^2 u(x)}{\partial x^2}\right)^2 dx - \frac{1}{2}\int_0^L F\left(\frac{\partial u}{\partial x}\right)^2 dx \tag{4}$$

$$\begin{aligned} u(x) &= A_1 \sin\frac{\pi x}{L} + A_0 \\ E(x) &= a_1 \sin\frac{\pi x}{L} + a_0 \end{aligned} \tag{5}$$

$$U = \frac{1}{2}\int_0^L E(x)\, I \left(\frac{\partial^2 u(x)}{\partial x^2}\right)^2 dx - Fu\left(\frac{L}{2}\right) \tag{6}$$

$$\begin{aligned} u(x) &= A_5x_5 + A_4x_4 + A_3x_3 + A_2x_2 + A_1x_1 + A_0 \\ E(x) &= a_4x_4 + a_3x_3 + a_2x_2 + a_1x_1 + a_0 \end{aligned} \tag{7}$$

Sinusoidal expressions are assumed for deflection and modulus of elasticity distributions of pinned-pinned column as depicted in Equations (5). To solve the unknown coefficients of $u(x)$ and $E(x)$, proper boundary conditions are utilized. The deflections at both ends should be zero, which ensures that A_0 is zero. On the other hand, the exact boundary value of E at the ends and mid-point are considered as minimum and maximum, respectively. With these assumptions, the constants of the $E(x)$ distribution are solved. Next, the following equation $\frac{\partial U}{\partial A_1} = 0$ can uphold the solution of the critical buckling load. On the contrary, the fifth and fourth order polynomial functions are assumed to represent the deflection and modulus of elasticity variations along the axially graded beam case as expressed in Equation (7). The six constant coefficients of the deflection equation are solved from four boundary conditions of the simply supported beam (the resisting moment by the supports or bending moment of the structures at two ends and deflection at two ends are zero) and two equations of $\frac{\partial U}{\partial A_i} = 0$. The constant coefficient values of the modulus of elasticity are solved similarly in the column case.

In both scenarios, the distribution of Young's modulus reaches a maximum at the midpoint of the span and a minimum at the left and right ends. However, the modulus variation follows a sinusoidal pattern for pinned-pinned columns and a polynomial function for simply supported beams. This ensures optimal structural stability within the given Young's modulus range. For column buckling, the modulus distribution and deflection at each point are first estimated, which enables the evaluation of the critical buckling load using the Rayleigh-Ritz method. In parallel, a column with a variable modulus of elasticity is modeled in Abaqus, which also provides the critical buckling load. Next, the deflection and critical load computed by these two methods are compared, as shown in Fig. 2 (c). On the other hand, the analysis for beam bending starts with the distribution of the modulus of elasticity and then estimates the deflection trends at various points. This information enables the accurate determination of the exact deflection using the Rayleigh-Ritz method. Concurrently, the beam can be modeled with a variable modulus of elasticity in Abaqus, which also calculates the deflection along its length. Later, these two results can be compared, as illustrated in Fig. 2 (d).

2. *FGM design: dual variable case*

In this case, a radially graded pressurized cylinder that is designed to enhance dimensional stability by utilizing the radial (σ_{11}) and tangential (σ_{22}) stress distributions is introduced. In this model, only internal pressure (p_i) is taken into account for modeling the cylinder. The radial and tangential stresses are formulated as depicted in Equation (8). According to these, the axial stress is independent of radius, and thus the radial and tangential stresses play a significant role in deforming the cylinder. Hence, the corresponding strain components can be minimized when the values of the stiffness matrix elements, C_{11} and C_{12}, are higher. The connecting line segment of two maximum points (C_{11}^{max}, C_{22}^{max}) of the property closure serves as the basis for constructing a function dependent on two stiffness parameters, as detailed in the linear trade-off equation (Equation (9)), where C_m and $(C_m + \Delta C)$ represent the minimum and maximum values, respectively.

$$\begin{aligned} \sigma_{11} &= \frac{r_i^2 p_i}{r_o^2 - r_i^2}\left(1 + \frac{r_o^2}{r^2}\right) \\ \sigma_{22} &= \frac{r_i^2 p_i}{r_o^2 - r_i^2}\left(1 - \frac{r_o^2}{r^2}\right) \end{aligned} \tag{8}$$

$$\begin{aligned} C_{11} &= C_m + \frac{|\sigma_{11}|}{|\sigma_{11}| + |\sigma_{22}|}\Delta C \\ C_{22} &= C_m + \frac{|\sigma_{22}|}{|\sigma_{11}| + |\sigma_{22}|}\Delta C \end{aligned} \tag{9}$$

After setting the stiffness matrix, the strain and displacement of the elements can be calculated analytically by Equations (10) and (11). To determine the strain components of the isotropic material, the stiffness matrix is considered constant throughout the radius whereas 10 different stiffness matrices are developed that correspond to each element for the FGM case. In the simulation process, the Abaqus finite element scheme is employed to analyze the stress, strain, and deformation of a pressurized cylinder subjected to internal pressure only. A radial discretization of the cylinder is modeled using 10 elements, with varying stiffness properties. These stiffness variations are derived from the relationship outlined in Equation (9), as referenced in the analytical case. This method allows for a detailed examination of the material's mechanical response, capturing localized effects and ensuring alignment with the analytical predictions.

$$[\varepsilon]_n = [C]_n^{-1}[\sigma]_n \tag{10}$$

$$u_1(n+1) = \sum_{i=0}^{n} \varepsilon_{11}(n)\Delta x_1 \tag{11}$$

III. Results and Discussion

A. Property closures for stiffness parameters

Exemplary property closures are developed to predict all possible values of stiffness parameters (C_{11}, C_{12}, C_{22}, and C_{66}), as well as Young's modulus (E_{11}) and Poisson's ratio (ν_{12}), of IN-718 alloy. The boundaries of closure are represented by the green discontinuous lines as shown in Fig. 3 and 4. These boundaries are obtained by solving the minimization problem, the objective function for optimizing the property closure of C_{ij} versus C_{kl} is defined as a minimization problem, aiming to minimize the absolute difference $|C_{ij} - C_{kl}|$ while satisfying the volume normalization constraint and fundamental non-negativity constraints for ODFs. Furthermore, the objective function can be modified to incorporate both maximization and minimization by setting the desired function $f(\mathbf{A})$ as C_{ij} or C_{kl}, allowing for the determination of local maximum and minimum values of specific stiffness matrix components, all while keeping the constraints unchanged. These local maximum and minimum points are exhibited by internally drawn black and blue curves as appeared in Fig. 3 and 4.. Eventually, the intersection point of these lines in each closure converges a randomly oriented texture providing isotropic properties. As a result, the intersection of the black and blue curves indicates that $C_{11} = C_{22} = C_{33} = 283.52$ GPa, $C_{12} = C_{13} = C_{23} = 117.05$ GPa, and $C_{44} = C_{55} = C_{66} = 82.52$ GPa, signifying an isotropic state where the probabilities (ODFs) of all texture components are equal. Moving away from this intersection point, the microstructure begins to exhibit non-isotropic properties, often transitioning into a transversely isotropic nature, where the probabilities of different texture components diverge. This divergence can be quantified by introducing a new term, *deviation*, as illustrated in Fig. 3. As we move further from the isotropic point, this deviation increases, reaching a maximum at a specific point that reflects the extreme behavior of a particular stiffness component.

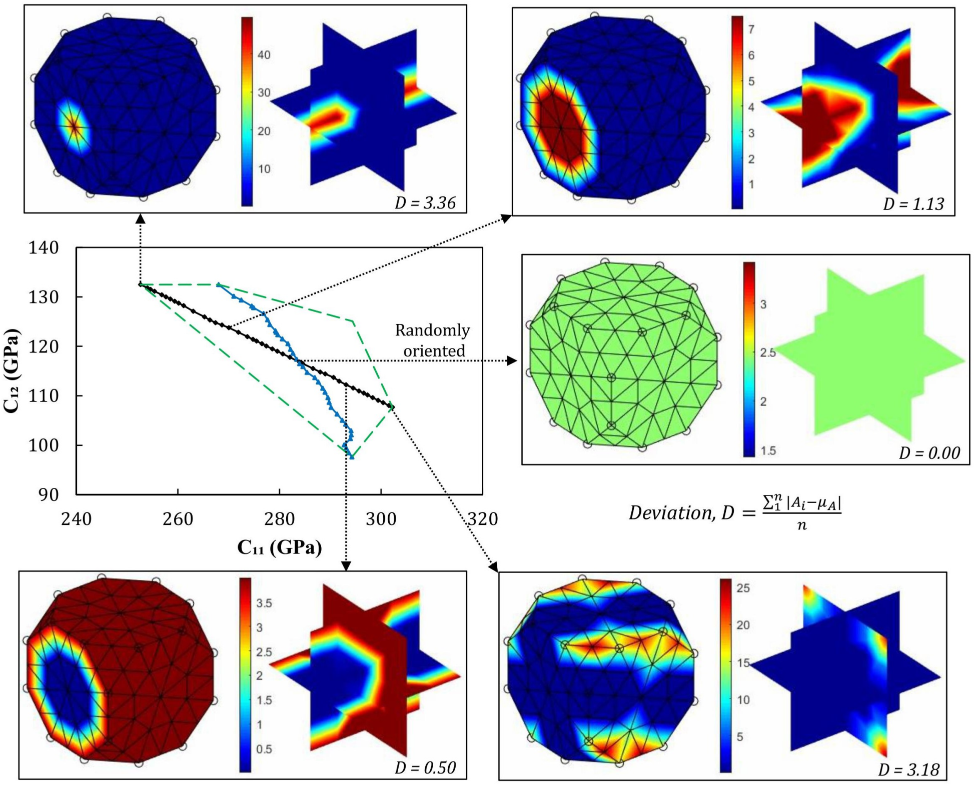

Fig. 3 Representation of microstructures along C_{11} minimization/maximization lines inside the closure of C_{11} versus C_{12} (ODFs are on Rodrigues orientation space).

The boundary points of the property closures represent extreme microstructures, where specific textures dominate with the highest probabilities compared to others. While these configurations may be theoretically conceivable, they are extremely challenging to produce experimentally. In contrast, points closer to the intersection of the black and blue curves correspond to more randomly oriented microstructures, which are generally less challenging to manufacture experimentally. One key observation from Fig. 4 is that the shape of the property closures remains consistent for similar sets of stiffness components. For instance, if the stiffness parameters are grouped as C_{11}, C_{22}, and C_{33}; C_{12}, C_{13}, and C_{23}; and C_{44}, C_{55}, and C_{66}, the property closures for C_{11} vs. C_{12} and C_{22} vs. C_{13} will appear similar. In other words, the stiffness components within the same group can be interchanged in Fig. 4, a property attributable to the material symmetry of cubic (FCC/BCC) structures. From Fig. 4 (c), it can be also observed that the property closure for a similar group of stiffness components, C_{11} vs C_{22}, is symmetric about a 45° line, indicating that they can be mutually interchanged. Additionally, another closure illustrating the relationship between E_{11} and ν_{12} is shown in Fig. 4(d). This closure can be mapped with the C_{11} vs. C_{12} closure, where the corner points of both closures represent the same microstructures. Interestingly, due to the crystal symmetry, the parameters E_{11}, E_{22}, and E_{33}; as well as ν_{12}, ν_{13}, and ν_{23} can be interchanged.

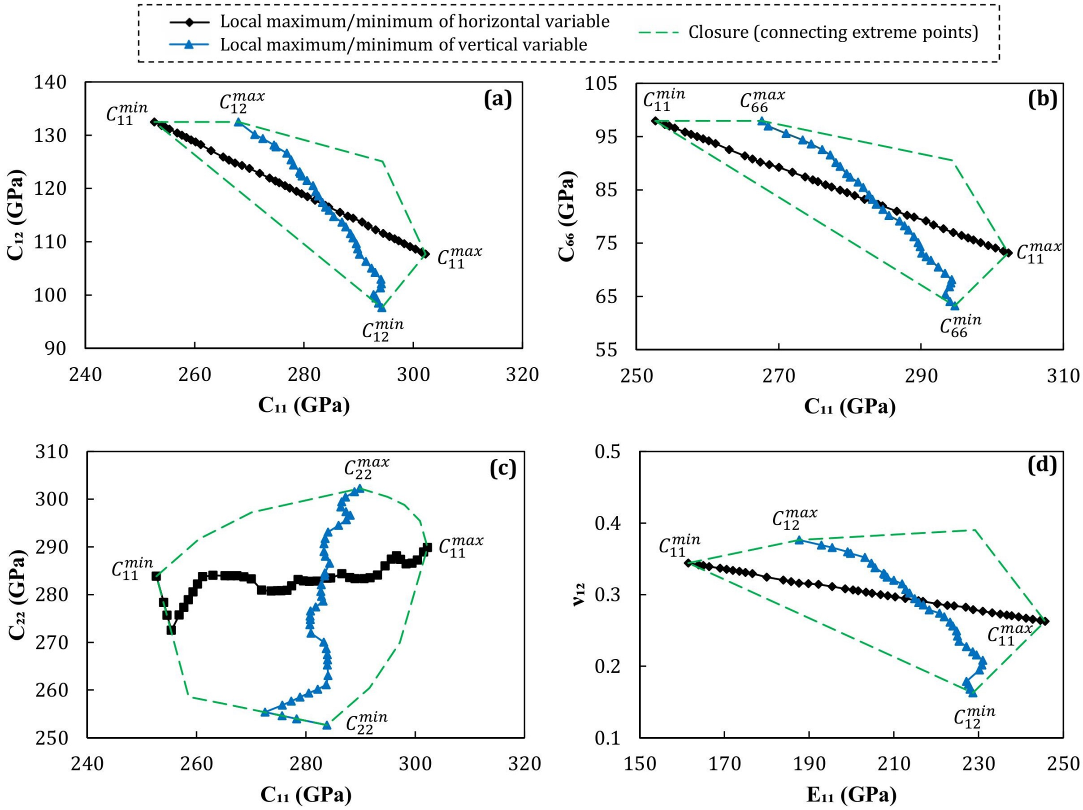

Fig. 4 Property closures of (a) C_{11} vs. C_{12}, (b) C_{11} vs. C_{66}, (c) C_{11} vs. C_{22} and (d) E_{11} vs. ν_{12}

B. Effect of uncertainty on property closures

The current section discusses the uncertainty in microstructural property closures arising from variations in microstructural textures (ODFs) and single-crystal properties. The ODF provides a probabilistic framework for representing grain orientations, and changes in one orientation influence others. Property closures are constructed based on the entire set of possible ODFs, ensuring that uncertainty in the ODF remains within the feasible material behavior space as appeared in Fig. 5 (a). If the points on the boundary of the closures are considered under the effects of the microstructural uncertainty, the resulting properties will shift but remain constrained within the closure, either on or inside the boundary. Similarly, if points are selected within the closures assumed under the effects of uncertainty, the resultant microstructure will exhibit properties that may shift in any direction, yet these too will remain confined within the closure. In contrast, uncertainty in single crystal properties directly influences closure size and shape. To simplify the analysis, the present work has focused on the uncertainty at the corner points of the closure, which define the new *stochastic* closure accounting for uncertainty. To capture the uncertainty propagation due to variations in single crystal properties, a 1% variation is introduced. This means two extreme scenarios are considered: one where all single crystal stiffness components are at their maximum and another where all are at their minimum. The revised closure, reflecting this uncertainty, is illustrated in Fig. 5 (b), with each corner representing four extreme uncertain points (a combination of $C_{ij} \pm \delta C_{ij}$). Here, δC_{ij} represents the propagated variation in any specific stiffness component C_{ij}, which depends on both the magnitude of C_{ij} at the point of interest and the percentage of variation applied to the single crystal properties. A larger C_{ij} and a higher variation percentage result in a greater δC_{ij}, and vice versa. Fig. 5 illustrates the uncertainty effect on the property closure for C_{11} versus C_{12} alone. Since the remaining property closures are similarly influenced by the propagated uncertainty, these are omitted to avoid redundant results.

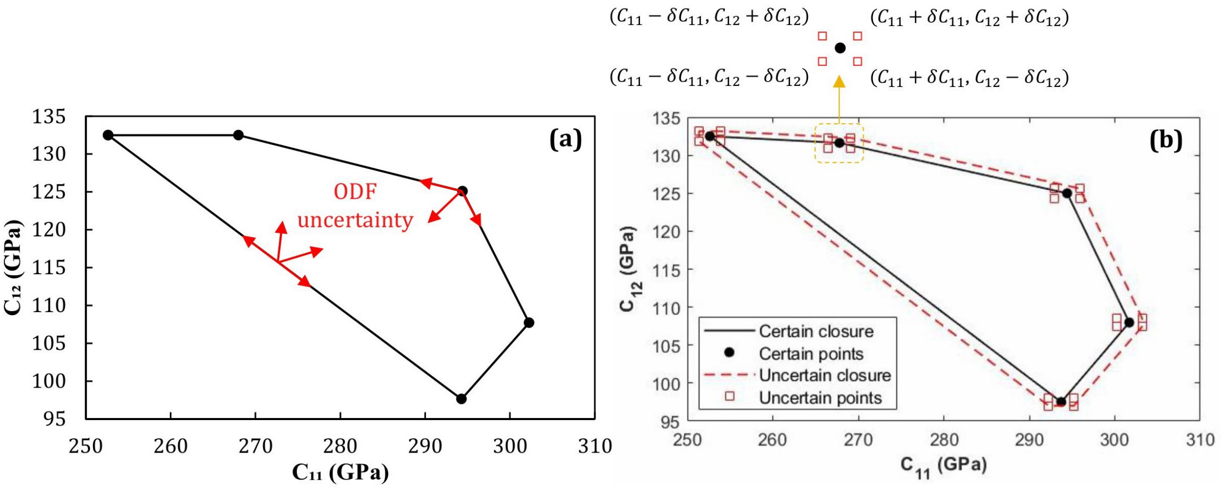

Fig. 5 Effect of uncertainty on the property closures of C_{11} vs. C_{12} for (a) Uncertain ODF and (b) Uncertain single crystal property (1% variation)

C. FGM structures

1. Single variable case

The Rayleigh-Ritz (R-R) method is employed to derive an optimal modulus of elasticity function, ensuring maximum stability for columns and beams. The modulus is set to vary between values corresponding to the randomly oriented microstructure and the maximum achievable modulus. However, the R-R derived modulus function assumes material isotropy, meaning $E_{11} = E_{22} = E_{33}$ at any given point, with these values changing along the x-axis according to the optimal function. In practice, the function is only applied to E_{11} in FGMs, as not all stiffness components can be adjusted by the same function. Specifically, as we move further from the intersection point of black and blue curves on property closures, the microstructure begins to exhibit transversely isotropic behavior ($C_{11} \neq C_{22} = C_{33}$). This makes it impractical to design an isotropic microstructure that follows a unified function. Therefore, in axially graded FGMs, the R-R driven function is primarily applied to E_{11}, as shown in Fig. 6 (a) and (b) depicting how stiffness components change with respect to x. Four distinct material models are considered, each assigned to a pinned-pinned column and a simply supported beam. A comprehensive overview of these four cases is concisely summarized in Table 1. The isotropic materials produced by the point A (intersection of blue and black lines in Fig. 4) microstructure are denoted by 'iso'. The analytical approach considers only variations in the modulus of elasticity, whereas the real scenario differs slightly, with all stiffness parameters varying throughout the AB (A to the maximum value of C_{11} in Fig. 4) line of the microstructures. This real scenario is denoted by AB-FGM, while the ideal FGM is denoted by iso-FGM. The beam and column have lengths, heights, and thicknesses of 50 cm, 4 cm, and 1 cm, respectively.

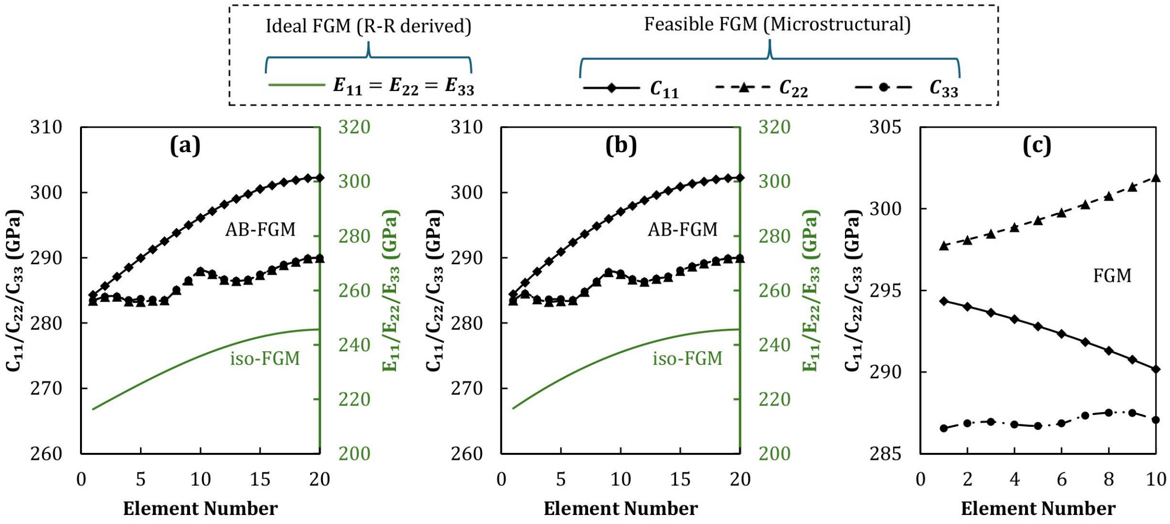

Fig. 6 Elastic stiffness components and modulus of elasticity with respect to corresponding elements; (a) Pinned-pinned column, (b) Simply supported beam, and (c) Radially graded pressurized cylinder.

Table 1 Summary of different beams/columns model and their characteristics

Short name	Presence on closures	Relations	Microstructures
iso-A	Intersection of black and blue curves	$E_{11} = E_{22} = E_{33} \neq f(x)$	Randomly oriented (shown in Fig. 3)
iso-FGM	Indirect (derived from R-R method)	$E_{11} = E_{22} = E_{33} = f(x)$	*Not applicable*
AB-FGM	Black curve (randomly oriented point to C_{11}^{max} or E_{11}^{max})	$E_{11} \neq E_{22} = E_{33}$ $E_{11} = f(x)$	Shown in 'Supplementary Materials'
B	Point of C_{11}^{max} or E_{11}^{max}	$E_{11} \neq E_{22} = E_{33}$ $E_{11} \neq f(x)$	Preferential orientations (shown in Fig. 3)

In analytical analysis, the R-R method is applied, whereas for FEA, the commercial package Abaqus is utilized. For both the pinned-pinned column and the simply supported beam, the structures are divided into a sufficient number of S8R elements to ensure an acceptable range of convergent results. The S8R element is an 8-node quadrilateral shell element with reduced integration, where each node possesses six degrees of freedom: three translations and three rotations. This element supports both geometric and material nonlinearities, making it acceptable for the current investigation. For the FGM structures, the model is divided into 40 equal portions, with the left 20 portions being symmetric to the right 20. The corresponding stiffness components are illustrated in Fig. 6 (a) and (b). The analytical and FEA results of the axially graded column and beam are illustrated in Fig. 7. Six distinct bars represent six specific outcomes under varying material or method conditions. For the beam, a 5 kN force is applied to examine the deflection under different material scenarios. The relative analysis, which calculates the increase in critical load and the reduction in maximum deflection, is performed with respect to isotropically produced structures using the R-R analytical method. This relative analysis offers dimension- and load-independent results, making it ideal for structural comparisons. In other words, changes in the applied load or dimensions of the beam and column do not affect these results. A comprehensive observation reveals that both the beam and column achieve greater stability when manufactured by the proposed FGM model. The axially graded (sinusoidal) pinned-pinned column can withstand ~ 13% higher load compared to the isotropic one and the graded (polynomial) simply-supported beam demonstrates ~ 12% lower deflection than the isotropic one. It is also observed that structures constructed with preferentially oriented microstructures (B) exhibit higher stability compared to others. However, the results from FGM demonstrate that it is not essential to use this extreme microstructure throughout the entire structure. In fact, it can often be more cost-effective to avoid constructing the whole structure with such microstructure.

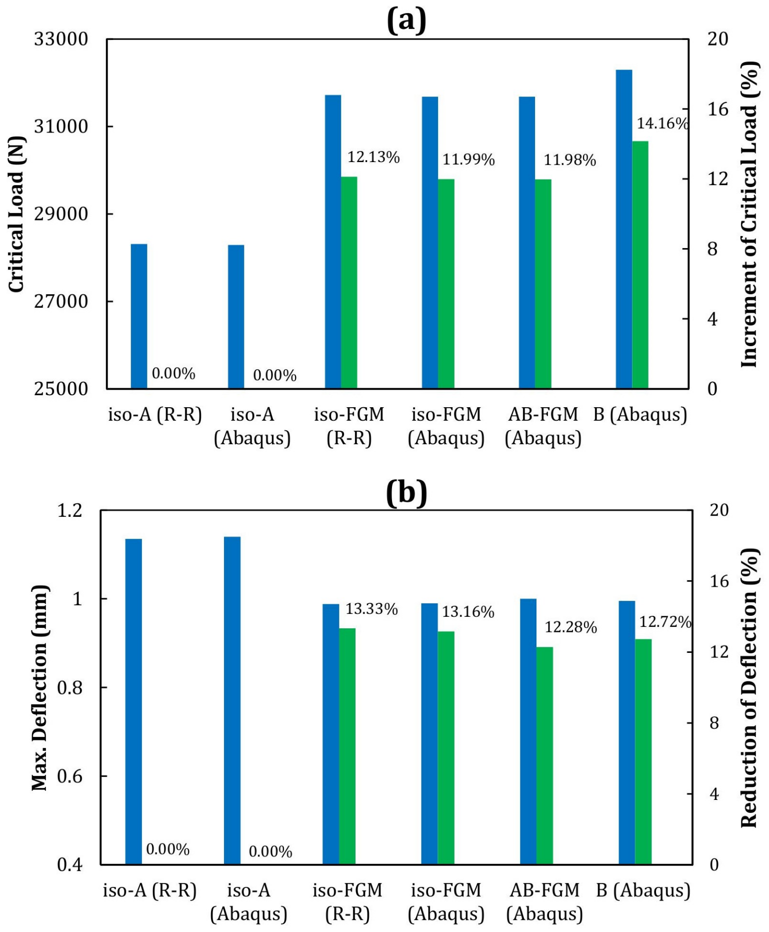

Fig. 7 Comparison of analytical method and FEA for (a) Pinned-pinned column, (b) Simply supported beam. (Blue bars correspond to left vertical axis and green bars correspond to right vertical axis)

2. *Dual variable case*

The analytical and FEA (Abaqus) results for the radially graded pressurized cylinder are depicted in Fig. 8 and 9, respectively. The cylinder has internal and outer radii of 10 mm and 15 mm, with only 200 MPa of internal pressure applied in this specific example. Analytically, the axial direction is not strain-free, despite zero applied stress in this direction; a small amount of axial strain develops due to the Poisson effect. However, the FEA under plain strain conditions demonstrates null axial strain. Since an infinitely long pressurized cylinder is considered, the strain in the longitudinal direction can be neglected. Consequently, the Abaqus FEA model employs a sufficient number of CPE8 elements to construct the cylinder's cross-section, ensuring that the result converges within an acceptable range. The CPE8 element is an 8-node quadrilateral element designed for plane strain analysis, making it particularly suitable for thick-walled pipes or pipes subjected to high internal pressure. The plane strain assumption implies that the strain normal to the pipe surface is negligible compared to the strains within the plane of the surface. Additionally, the quadrilateral shape of the CPE8 element provides a more accurate representation of curved geometries. For the isotropic structure, the entire cylindrical section is assumed to be composed of a randomly oriented microstructure, resulting in a perfectly isotropic behavior. In contrast, for the radially graded FGM cylinder, the model is segmented into 10 equal portions along the radial direction. The stiffness components corresponding to these sections are depicted in Fig. 6 (c), where C_{11} and C_{22} adhere to a linear trade-off equation based on the radial and hoop stress distributions. The microstructures connecting the two points of maximum C_{11} and C_{22} in Fig. 4 (c) are utilized to construct the radially graded cylinder. Since C_{11} and C_{22} are selected simultaneously, there is no control over C_{33}, which also exhibits slight variations along the radial direction. The detailed microstructures along the radial direction can be accessed in the 'Supplementary Materials' section. The comprehensive observation from these two different analyses confirms that the proposed FGM structures can significantly reduce cylinder deformation under the specified loading conditions. The proposed radially graded pressurized cylinder can exhibit ~ 16% and ~ 13% more dimensional stability according to the results of the analytical method and FEA, respectively, under internal pressure.

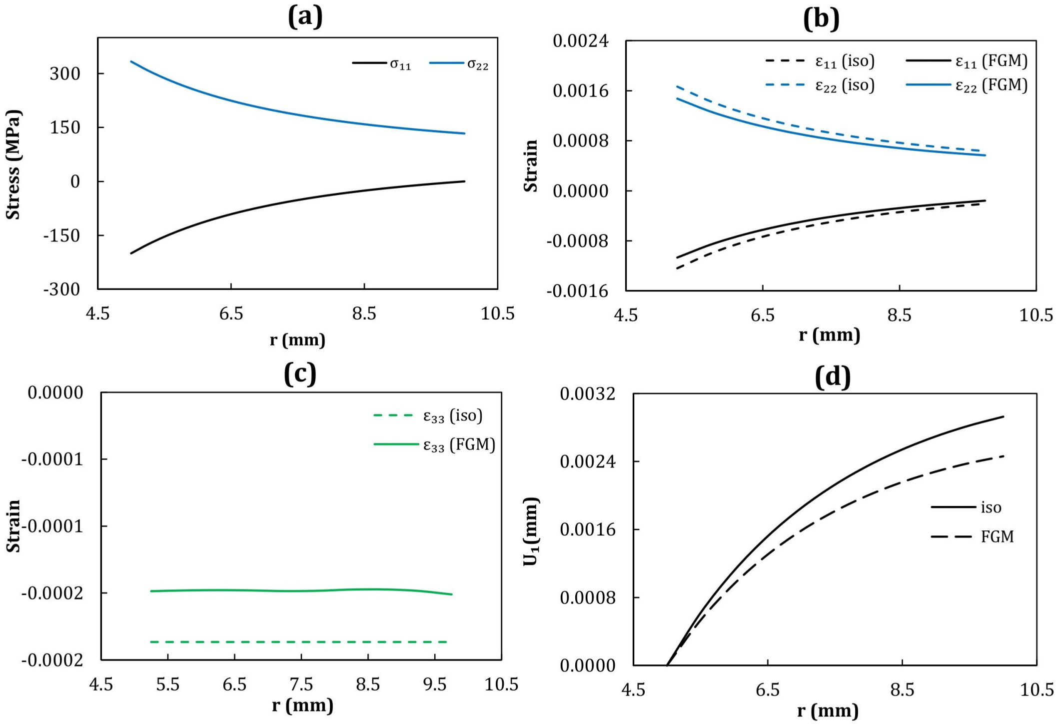

Fig. 8 Results for the radially graded pressurized cylinder obtained by the analytical approach (a) Stress distributions, (b)-(c) Strain distributions, and (d) Radial displacements.

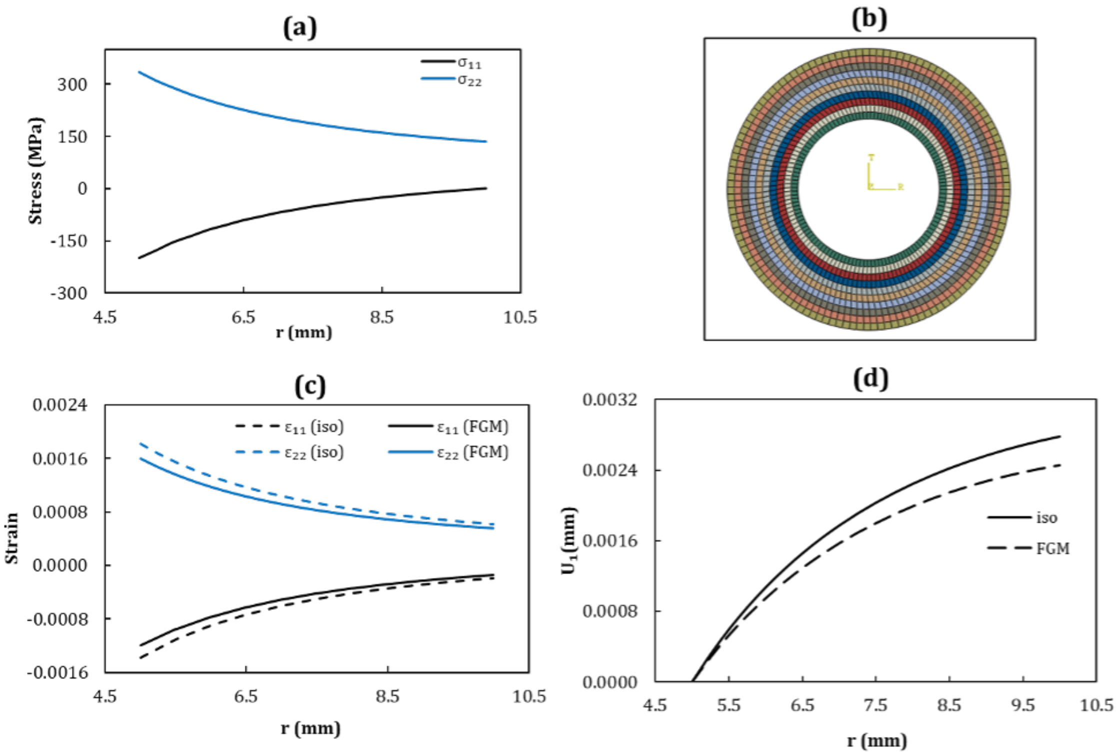

Fig. 9 Results for the radially graded pressurized cylinder obtained by FEA (a) Stress distributions and (b) Sections and FEA mesh (different colors represent grading on properties), (c) Strain distributions, and (d) Radial displacements.

IV. Conclusion

This study has established property closures for stiffness parameters of polycrystalline IN-718 by investigating the effects of microstructural texture variations. The analysis also includes the impact of uncertainties in single-crystal properties and microstructural texture on these property closures. By leveraging the computed property closures, several designs have been proposed for functionally graded structures that demonstrate enhanced dimensional stability under specific loading conditions. The functionally graded structures can be designed with specific objectives such as optimization of stress distributions and minimization of strains while adhering to constraints associated with material property closures demonstrating all possible values of properties obtainable by any feasible microstructural texture. The presented design approach in this study is found to be promising for enhancing structural performance across various applications. Accordingly, the proposed designs, including a radially graded pressurized cylinder, an axially graded (sinusoidal) pinned-pinned column, and an axially graded (polynomial) simply supported beam, showcase notable improvements. It is also observed that structures constructed with preferentially oriented microstructures exhibit higher stability compared to other configurations. However, findings from FGMs reveal that it is not essential to apply these extreme microstructural orientations uniformly across the entire structure. FGMs demonstrate the ability to deliver comparable performance by strategically varying the material properties, which leads to a more efficient design without the need for achieving specific (and biased) orientations. This flexibility in the microstructure can help optimize both performance and material use, making FGMs a more versatile option.

Supplementary Materials

The ODFs in Rodrigues orientation space and the <111>, <100> and <110> pole figures of the microstructures used for both single-variable and dual-variable FGMs can be accessed from this GitHub link:

https://github.com/MARUF087/Microstructures-of-FGM-structures.git

Acknowledgments

The authors acknowledge the financial support from the National Science Foundation (NSF) under award numbers 2053840 and 2328112.

References

[1] Pollock, T., Clarke, A., and Babu, S., "Design and tailoring of alloys for additive manufacturing," *Metallurgical and Materials Transactions A*, Vol. 51, 2020, pp. 6000–6019.

[2] Gu, D. D., Meiners, W., Wissenbach, K., and Poprawe, R., "Laser additive manufacturing of metallic components: materials, processes and mechanisms," *International materials reviews*, Vol. 57, No. 3, 2012, pp. 133–164.

[3] Yong, C. K., Gibbons, G. J., Wong, C. C., and West, G., "A critical review of the material characteristics of additive manufactured IN718 for high-temperature application," *Metals*, Vol. 10, No. 12, 2020, p. 1576.

[4] Hosseini, E., and Popovich, V., "A review of mechanical properties of additively manufactured Inconel 718," *Additive Manufacturing*, Vol. 30, 2019, p. 100877.

[5] Schafrik, R. E., Ward, D. D., and Groh, J. R., "Application of alloy 718 in GE aircraft engines: past, present and next five years," *Superalloys*, Vol. 718, No. 625, 2001, pp. 1–11.

[6] Billah, M. M., and Acar, P., "Design of polycrystalline metallic alloys under multi-scale uncertainty by connecting atomistic to meso-scale properties," *Acta Materialia*, Vol. 270, 2024, p. 119879.

[7] Acar, P., and Sundararaghavan, V., "Utilization of a linear solver for multiscale design and optimization of microstructures," *AIAA Journal*, Vol. 54, No. 5, 2016, pp. 1751–1759.

[8] Hasan, M., and Acar, P., "Machine learning reinforced microstructure-sensitive prediction of material property closures," *Computational Materials Science*, Vol. 210, 2022, p. 110930.

[9] Acar, P., "Computational Design of Microstructures With Stochastic Property Closures," *Journal of Engineering Materials and Technology*, Vol. 143, No. 1, 2021, p. 011008.

[10] Adams, B. L., Gao, X. C., and Kalidindi, S. R., "Finite approximations to the second-order properties closure in single phase polycrystals," *Acta Materialia*, Vol. 53, No. 13, 2005, pp. 3563–3577.

[11] Kalidindi, S. R., Binci, M., Fullwood, D., and Adams, B. L., "Elastic properties closures using second-order homogenization theories: case studies in composites of two isotropic constituents," *Acta Materialia*, Vol. 54, No. 11, 2006, pp. 3117–3126.

[12] Proust, G., and Kalidindi, S. R., "Procedures for construction of anisotropic elastic–plastic property closures for face-centered cubic polycrystals using first-order bounding relations," *Journal of the Mechanics and Physics of Solids*, Vol. 54, No. 8, 2006, pp. 1744–1762.

[13] Landry, N. W., and Knezevic, M., "Delineation of first-order elastic property closures for hexagonal metals using fast fourier transforms," *Materials*, Vol. 8, No. 9, 2015, pp. 6326–6345.

[14] Mann, A., and Kalidindi, S. R., "Development of a robust CNN model for capturing microstructure-property linkages and building property closures supporting material design," *Frontiers in materials*, Vol. 9, 2022, p. 851085.

[15] Yadroitsev, I., Shishkovsky, I., Bertrand, P., and Smurov, I., "Manufacturing of fine-structured 3D porous filter elements by selective laser melting," *Applied Surface Science*, Vol. 255, No. 10, 2009, pp. 5523–5527.

[16] Popovich, V., Borisov, E., Popovich, A., Sufiiarov, V. S., Masaylo, D., and Alzina, L., "Functionally graded Inconel 718 processed by additive manufacturing: Crystallographic texture, anisotropy of microstructure and mechanical properties," *Materials & Design*, Vol. 114, 2017, pp. 441–449.

[17] Mumtaz, K., and Hopkinson, N., "Selective laser melting of thin wall parts using pulse shaping," *Journal of Materials Processing Technology*, Vol. 210, No. 2, 2010, pp. 279–287.

[18] Popovich, A. A., Sufiiarov, V. S., Polozov, I. A., and Borisov, E. V., "Microstructure and mechanical properties of Inconel 718 produced by SLM and subsequent heat treatment," *Key Engineering Materials*, Vol. 651, 2015, pp. 665–670.

[19] Song, B., Dong, S., Coddet, P., Liao, H., and Coddet, C., "Fabrication of NiCr alloy parts by selective laser melting: columnar microstructure and anisotropic mechanical behavior," *Materials & Design*, Vol. 53, 2014, pp. 1–7.

[20] Liu, X., Wang, K., Hu, P., He, X., Yan, B., and Zhao, X., "Formability, microstructure and properties of inconel 718 superalloy fabricated by selective laser melting additive manufacture technology," *Materials*, Vol. 14, No. 4, 2021, p. 991.

[21] Thijs, L., Sistiaga, M. L. M., Wauthle, R., Xie, Q., Kruth, J.-P., and Van Humbeeck, J., "Strong morphological and crystallographic texture and resulting yield strength anisotropy in selective laser melted tantalum," *Acta Materialia*, Vol. 61, No. 12, 2013, pp. 4657–4668.

[22] Ni, M., Chen, C., Wang, X., Wang, P., Li, R., Zhang, X., and Zhou, K., "Anisotropic tensile behavior of in situ precipitation strengthened Inconel 718 fabricated by additive manufacturing," *Materials Science and Engineering: A*, Vol. 701, 2017, pp. 344–351.

[23] Segersäll, M., and Moverare, J. J., "Crystallographic orientation influence on the serrated yielding behavior of a single-crystal superalloy," *Materials*, Vol. 6, No. 2, 2013, pp. 437–444.

[24] Moverare, J. J., Johansson, S., and Reed, R. C., "Deformation and damage mechanisms during thermal–mechanical fatigue of a single-crystal superalloy," *Acta Materialia*, Vol. 57, No. 7, 2009, pp. 2266–2276.

[25] Miyamoto, Y., Kaysser, W., Rabin, B., Kawasaki, A., and Ford, R. G., *Functionally graded materials: design, processing and applications*, Vol. 5, Springer Science & Business Media, 2013.

[26] Gupta, A., and Talha, M., "Recent development in modeling and analysis of functionally graded materials and structures," *Progress in Aerospace Sciences*, Vol. 79, 2015, pp. 1–14.

[27] Chen, D., Gao, K., Yang, J., and Zhang, L., "Functionally graded porous structures: Analyses, performances, and applications–A Review," *Thin-Walled Structures*, Vol. 191, 2023, p. 111046.

[28] Tutuncu, N., and Ozturk, M., "Exact solutions for stresses in functionally graded pressure vessels," *Composites Part B: Engineering*, Vol. 32, No. 8, 2001, pp. 683–686.

[29] Bezzie, Y. M., and Woldemichael, D. E., "Effects of graded-index and Poisson's ratio on elastic-solutions of a pressurized functionally graded material thick-walled cylinder," *Forces in Mechanics*, Vol. 4, 2021, p. 100032.

[30] Sburlati, R., "Analytical elastic solutions for pressurized hollow cylinders with internal functionally graded coatings," *Composite Structures*, Vol. 94, No. 12, 2012, pp. 3592–3600.

[31] Ranganathan, S. I., Abed, F. H., and Aldadah, M. G., "Buckling of slender columns with functionally graded microstructures," *Mechanics of Advanced Materials and Structures*, Vol. 23, No. 11, 2016, pp. 1360–1367.

[32] Şimşek, M., Kocatürk, T., and Akbaş, Ş., "Dynamic behavior of an axially functionally graded beam under action of a moving harmonic load," *Composite Structures*, Vol. 94, No. 8, 2012, pp. 2358–2364.

[33] Li, X., Li, L., Hu, Y., Ding, Z., and Deng, W., "Bending, buckling and vibration of axially functionally graded beams based on nonlocal strain gradient theory," *Composite Structures*, Vol. 165, 2017, pp. 250–265.

[34] Babilio, E., "Dynamics of an axially functionally graded beam under axial load," *The European Physical Journal Special Topics*, Vol. 222, No. 7, 2013, pp. 1519–1539.

[35] El-Ashmawy, A., Kamel, M., and Elshafei, M. A., "Thermo-mechanical analysis of axially and transversally Function Graded Beam," *Composites part B: Engineering*, Vol. 102, 2016, pp. 134–149.

[36] Sundararaghavan, V., and Zabaras, N., "Linear analysis of texture–property relationships using process-based representations of Rodrigues space," *Acta materialia*, Vol. 55, No. 5, 2007, pp. 1573–1587.

[37] Kumar, A., and Dawson, P., "Computational modeling of FCC deformation textures over Rodrigues' space," *Acta Materialia*, Vol. 48, No. 10, 2000, pp. 2719–2736.

[38] Cho, J.-H., "Determination of volume fraction of the texture components in the Rodrigues fundamental region," *Materials Science and Engineering: A*, Vol. 465, No. 1-2, 2007, pp. 228–237.

[39] Kumar, A., and Dawson, P. R., "Modeling crystallographic texture evolution with finite elements over neo-Eulerian orientation spaces," *Computer methods in applied mechanics and engineering*, Vol. 153, No. 3-4, 1998, pp. 259–302.

[40] Houtte, P. V., et al., "On the representation of texture functions of cubic metals in Euler space," *Texture, Stress, and Microstructure*, Vol. 7, 1987, pp. 187–205.

[41] Cho, J.-H., Rollett, A., and Oh, K., “Determination of volume fractions of texture components with standard distributions in Euler space,” *Metallurgical and Materials Transactions A*, Vol. 35, 2004, pp. 1075–1086.

[42] Acar, P., “Reliability-based design optimization of microstructures with analytical formulation,” *Journal of Mechanical Design*, Vol. 140, No. 11, 2018, p. 111402.

[43] Haldipur, P., *Material characterization of nickel-based super alloys through ultrasonic inspection*, Iowa State University, 2006.

[44] Ilanko, S., Monterrubio, L., and Mochida, Y., *The Rayleigh-Ritz method for structural analysis*, John Wiley & Sons, 2014.